Lawrence Berkeley National Laboratory

LBL Publications

Title

An Electrochemical, Microtopographical and Ambient Pressure X-Ray Photoelectron Spectroscopic Investigation of Si/TiO2/Ni/Electrolyte Interfaces

Permalink

https://escholarship.org/uc/item/9kh560vf

Journal

Journal of The Electrochemical Society, 163(2)

ISSN

0013-4651

Authors

Lichterman, Michael F
Richter, Matthias H
Hu, Shu
et al.

Publication Date

2016

DOI

10.1149/2.0861602jes

Peer reviewed

eScholarship.org Powered by the California Digital Library
University of California

An Electrochemical, Microtopographical and Ambient Pressure-X-ray Photoelectron Spectroscopic Investigation of $Si/TiO_2/Ni$/Electrolyte Interfaces

Michael F. Lichterman[a,b]*, Matthias H. Richter[a,b]*, Shu Hu[a,b]*, Ethan J. Crumlin[c]*, Stephanus Axnanda[c], Marco Favaro[c,d,e], Walter Drisdell[d,e], Zahid Hussain[c], Bruce S. Brunschwig[b,f], Nathan S. Lewis[a,b,f,g], Zhi Liu[c,h,i], and Hans-Joachim Lewerenz[b‡]

[a] Division of Chemistry and Chemical Engineering, California Institute of Technology, Pasadena, CA 91125, USA.

[b] Joint Center for Artificial Photosynthesis, California Institute of Technology, Pasadena, CA 91125, USA.

[c] Advanced Light Source, Lawrence Berkeley National Laboratory, Berkeley, CA 94720, USA

[d] Materials Science Division, Lawrence Berkeley National Laboratory, Berkeley, CA 94720, USA

[e] Joint Center for Artificial Photosynthesis, Lawrence Berkeley National Laboratory, Berkeley, CA 94720, USA

[f] Beckman Institute, California Institute of Technology, Pasadena, CA 91125, USA

[g] Kavli Nanoscience Institute, California Institute of Technology, Pasadena, CA 91125, USA.

[h] State Key Laboratory of Functional Materials for Informatics, Shanghai Institute of Microsystem and Information Technology, Chinese Academy of Sciences, Shanghai 200050, China.

[i] School of Physical Science and Technology, ShanghaiTech University, Shanghai 200031, China.

‡ Corresponding author E-mail: lewerenz@caltech.edu

* These authors contributed equally to the work. MFL, MHR and SH contributed to the design, execution, and analysis of the experiment; EJC was critical in the design, building and testing of the end station that allows atmospheric pressure XPS data collection on a solution under potentiostatic control.

Abstract

The electrical and spectroscopic properties of the TiO_2/Ni protection layer system, which enables stabilization of otherwise corroding photoanodes, have been investigated in contact with electrolyte solutions by scanning-probe microscopy, electrochemistry and *in-situ* ambient pressure X-ray photoelectron spectroscopy (AP-XPS). Specifically, the energy-band relations of the p^+-Si/ALD-TiO_2/Ni interface have been determined for a selected range of Ni thicknesses. AP-XPS measurements using tender X-rays were performed in a three-electrode electrochemical arrangement under potentiostatic control to obtain information from the semiconductor near-surface region, the electrochemical double layer (ECDL) and the electrolyte beyond the ECDL. The degree of conductivity depended on the chemical state of the Ni on the TiO_2 surface. At low loadings of Ni, the Ni was present primarily as an oxide layer and the samples were not conductive, although the TiO_2 XPS core levels nonetheless displayed behavior indicative of a metal-electrolyte junction. In contrast, as the Ni thickness increased, the Ni phase was primarily metallic and the electrochemical behavior became highly conductive, with the AP-XPS data indicative of a metal-electrolyte junction. Electrochemical and microtopographical methods have been employed to better define the nature of the TiO_2/Ni electrodes and to contextualize the AP-XPS results.

Introduction

Photoelectron spectroscopy can be used to directly characterize the energy relations of semiconductor/liquid junctions that underlie the operation of photoelectrochemical cells [1], provided that the kinetic energy of the emitted photoelectrons can elastically penetrate the water film on the electrode surface. Conventional X-ray photoelectron spectroscopy (XPS) experiments are performed in ultra-high vacuum (UHV) in the absence of electrolyte, and thus do not allow for electrochemical control of an operating device during collection of XPS data. Recent theoretical work has shown that the inclusion of structured solvation layers on electrodes can alter the surface dipole by 0.5 – 0.7 eV (1.9 – 2.1 eV) for IrO_2 (WO_3) [2]. Established *in-system* techniques that allow analyses of (photo)electrodes after electrochemical operation enable assessment of aspects of the surface chemistry and of the associated energetic behavior [3-5]. However, such experiments are limited in scope and interpretation due to the rinsing, drying and outgassing procedures required prior to insertion of the sample into the UHV analysis chamber. In contrast, the use of tender X-rays having photon energies in the 2.3 – 5.2 keV energy range allows generation of photoelectrons that have a substantially increased inelastic mean free path. This approach allows "operando" XPS studies in conjunction with a classical three-electrode potentiostatic arrangement and also facilitates investigation of the influence of the applied potential on the band-edge energies of metal, semiconductor and hybrid electrodes at such interfaces [6,7]. Band bending and band-edge shifts can thus be determined directly by this spectroscopic technique [7].

We describe herein surface-sensitive analysis techniques for the characterization of TiO_2/Ni/electrolyte interfaces. The protection and stabilization of photoanodes for water oxidation to O_2(g) is of interest because high performance and stability can be achieved simultaneously by protecting a variety of otherwise unstable semiconductor photoanodes [8-11].

72 Specifically, TiO_2 has been used as a protection layer for photoelectrodes in either alkaline or
73 acidic media [7,12-17]. Some work indicates that annealing the TiO_2 allows for charge conduction
74 with minimal band bending, with unannealed TiO_2 preferred for photocathodes. However, the
75 role of the metallization layer in determining the charge-conduction properties of the films has
76 not been well elucidated [18]. A thin layer of TiO_2 can protect Si and allows for water oxidation
77 with an Ir oxygen-evolution catalyst, but in such systems increases beyond 2 nm in the thickness
78 of the TiO_2 film led to a substantial increase in resistance, such that a 10 nm film was nearly
79 nonconductive even when contacted with Ir [11]. In contrast, TiO_2 has been found to be a nearly
80 ideal protection layer from the viewpoint of the band-edge alignment when used on p-InP or p-Si
81 photocathodes [19,20]. Thus, while the band positions of the TiO_2 films appear to be inherently
82 conducive to photocathode protection, the nature of the TiO_2/(metal)/electrolyte contact requires
83 further investigation. Specifically, when contacted with Ni metal, TiO_2 films allow for the
84 sustained use of highly efficient semiconductor materials (Si, III-V, II-VI) for water splitting and
85 in other oxidizing environments, especially in alkaline media where efficient, intrinsically safe
86 solar-driven water-splitting systems can be built [12,13].

87 We describe herein the use of a three-electrode photoelectrochemical cell that contains a
88 meniscus-based ~ 13 nm thick electrolyte on the working electrodes formed from p^+-Si/TiO_2/Ni
89 interfaces, which allows XPS measurements under electrochemical control through the solution
90 [6,7]. Combined electrochemistry-photoelectron spectroscopic data that extend the previous
91 characterization of this system [7] have been collected in this work.

92 Degenerately doped Si was used as a back contact for the TiO_2 to ensure that the changes
93 in the observed binding energies originated from electric fields (or their absence) in the TiO_2 and
94 not in the underlying Si. (Photo)electrochemical and microtopographical characterization using
95 scanning probe microscopy have additionally been performed to assess the nature of the electrode

96 surfaces and their conductivity properties as a function of the amount of metal deposited onto the
97 TiO_2-coated photoanode surface. Recent work [15] in addition to work from our labs [7,12,13,17]
98 suggests that the presence or absence of band bending is a key factor for facilitating charge
99 conduction through these films. The experiments reported herein demonstrate that the degree of
100 band-bending in a semiconductor (photo)electrode is not the only parameter that allows for
101 charge conduction. The data also indicate that metallization that decreases the band bending is
102 necessary for conduction. Hence multiple parameters must be optimized to obtain a functional
103 protected photoelectrode.
104

105 # Experimental

106 Films of TiO_2 were produced by atomic-layer deposition (ALD) [12,13,21,22] on degenerately
107 doped p-type silicon ("p^+-Si") substrates. (100)-oriented boron doped Si wafers with a resistivity
108 $\rho < 0.005$ Ω·cm were first cleaned *via* an oxidizing etch, with the Si soaked for 2 min in a 3:1 (by
109 volume) "piranha" solution of concentrated H_2SO_4 (98 %) to 30 % H_2O_2(aq), followed by an etch
110 for 10 s in a 10 % (by volume) solution of HF(aq). The wafers were then immediately etched in a
111 5:1:1 (by volume) solution of H_2O, 36 % hydrochloric acid, and 30 % hydrogen peroxide for
112 10 min at 75 °C before being moved into the ALD chamber. The TiO_2 was deposited from a
113 tetrakis(dimethylamido)titanium (TDMAT) precursor in a Cambridge Nanotech Savannah ALD
114 reactor. In an ALD cycle, a 0.1 s pulse of TDMAT was followed by a 15 s purge of N_2 at
115 20 sccm, followed by a 0.015 s pulse of H_2O before another 15 s purge with N_2. This process was
116 repeated for 1500 cycles to provide films ~ 70 nm in thickness. Where desired, Ni was deposited
117 at a rate of ~ 2 nm per min by use of a RF sputtering power of 150 W for 20 s – 300 s in an AJA-
118 International sputtering system. The time used to sputter the Ni is denoted herein as t_{sp}.

119 Atomic-force microscopy (AFM) data were collected using a Bruker Dimension Icon
120 AFM, using Peakforce Quantitative Nanomechanical parameters, to provide information on the
121 height, adhesion and deformation of the sample surface. ScanAsyst mode was used to optimize
122 the tapping frequency and other experimental parameters, e.g. the gain, set point, and cantilever
123 tuning. ScanAsyst-Air tips (silicon nitride) were used, with a nominal tip radius of 2 nm and a
124 rotated (symmetric) geometry.

125 Electrochemical characterization was performed at a scan rate of 50 mV s^{-1} in either
126 1.0 M KOH(aq) or 50/350 mM $Fe(CN)_6^{3-/4-}$(aq), using Biologic SP-200 and SP-300 potentiostats.
127 In KOH, a leak-free Ag/AgCl reference electrode (eDAQ) and a platinum counter electrode were
128 used. For measurements in $Fe(CN)_6^{3-/4-}$(aq), the reference and counter electrodes were each Pt
129 mesh electrodes.

130 *Operando* AP-XPS experiments were performed at the Advanced Light Source, Berkeley
131 at the tender X-ray beamline 9.3.1 [6,7]. Fig. 1 presents schematically the geometry of the end
132 station. Potentials were applied between the reference electrode, E_{REF}, and the Fermi energy, E_F,
133 of the working electrode. X-rays at an energy of 4 keV were selected from a range of 2.3 keV –
134 5.2 keV with an energy resolution of $E/\Delta E$ = 3000-7200. The X-ray beam spot size at the beam
135 line was 1 mm x 2 mm [6]. The photoelectron collection cone was aligned to the beam line X-ray
136 spot at a distance of ~ 300 μm (Fig. 1). The experiments were performed using an
137 electrochemical cell with a hanging meniscus "emersion" configuration. Negligible steady-state
138 faradaic current was passed at the potentials used in the experiments described herein. We
139 designate this condition as "*operando*" because the observed region of the working electrode was
140 under potential control and the working electrode itself comprised an isopotential surface. The
141 pressure in the sample chamber was between 20 and 27 mbar, which is considered ambient
142 pressure in the context of X-ray spectroscopy. To prepare electrodes for *operando* AP-XPS, strips

143 of the p^+-Si/TiO_2/(Ni) wafers were cut into 1 cm x 3.5 cm rectangles. Highly doped p^+-Si was
144 used simultaneously as a support material as well as to provide an effective back contact to the
145 ALD-TiO_2. The ohmic contact at the back of the semiconductor was connected to the
146 photoelectron analyzer to provide a high conductivity ground for the sample. To make ohmic
147 contact to the sample, an In/Ga eutectic was scribed into the back of the Si wafer, and Ag paint
148 was used to contact the electrode to a strip of Cu tape that was supported on a 0.8 cm x 3 cm
149 glass slide.
150

151 # Results

152 TiO_2/Ni/electrolyte structures having varying thicknesses of Ni were analyzed in detail.
153 The Ni thickness is referred to by the sputter deposition time, t_{sp}, as described in the experimental
154 section. For short deposition times, the Ni films were incomplete and non-uniform. Thus, the
155 deposition time is more informative than a calculated thickness, and hence t_{sp} has been quoted
156 herein as the independent variable that was varied experimentally to produce the different
157 interfaces under study.
158

159 **Electrochemical Characterization**

160 Deposition of Ni onto relatively thick (44 nm to 150 nm) ALD-grown TiO_2 enables
161 charge conduction through the TiO_2 [12,13]. In previous photoelectrochemical analyses [12,13], Ni
162 deposits consisted either of large islands (3 x 7 micron grid) or of thin, t_{sp} ~ 120 s, sputtered Ni
163 films. Herein we investigate the characteristics of interfaces formed by deposition of a variety of
164 Ni layer thicknesses.

165 Fig. 2a shows the current density vs. potential (*J-U)* characteristics of TiO_2/Ni electrodes
166 in 1.0 M KOH formed using Ni deposition times of 0 s, 20 s, 60 s, or 300 s. The *J-U* sweeps were

167 initiated in the positive direction from the open-circuit potential, U_{OC}. The data were recorded
168 after completion of the AP-XPS measurements, to establish the interrelation of the
169 voltammograms with the photoelectron spectra. Five main features were observed in the
170 voltammetric data for TiO_2/Ni (60 s) and TiO_2/Ni (300 s) interfaces. For t_{sp} = 60 s, the onset of
171 hydrogen evolution (HER) occurred at -1.1 V vs. Ag/AgCl, and an anodic peak, wave A, was
172 observed at U = -0.7 V vs. Ag/AgCl, attributable to the oxidation of metallic Ni(0) to Ni(II) [23].
173 The related cathodic peak associated with the reduction of Ni(II) to Ni(0) was not observed. At
174 positive potentials, the J-U data exhibited an oxidative transformation at U = +0.39 V (wave B;
175 anodic current) ascribable to Ni(II) to Ni(III), prior to the onset of the oxygen-evolution reaction
176 (OER) at +0.52 V vs. Ag/AgCl. A reductive peak at U = +0.23 V vs. Ag/AgCl (wave C; cathodic
177 current) was observed on the return sweep. For t_{sp} = 300 s, the anodic and cathodic waves at
178 +0.34 V and +0.28 V vs. Ag/AgCl, respectively, exhibited less separation, and the catalytic OER
179 current was observed at 0.49 V vs. Ag/AgCl. The samples that had lower catalyst loadings, e.g.
180 t_{sp} = 20 s, did not display the Ni(0)/Ni(II) and Ni(II)/Ni(III) redox peaks.
181 Fig. 2b shows the electrochemical data obtained when the electrodes were in contact with
182 $Fe(CN)_6^{3-/4-}$(aq). An analogous trend was observed, and only electrodes with Ni thicknesses of
183 > 2 nm (sputter times ≥ 60s) exhibited substantial current flow, even in the presence of an
184 electrochemically reversible one-electron redox couple.
185
186 **Surface Microtopography**
187 Tapping mode AFM data were obtained to determine the coverage and structure of the Ni
188 overlayer (Fig. 3). Only minor differences (~ 4 %) in roughness between bare TiO_2 and TiO_2 with
189 t_{sp} = 20 s or 60 s of Ni deposition (Table 1) were observed in the sample height data obtained
190 using peak force quantitative nanomechanical measurements (Fig. 3a). However, a local

191 minimum in deformation was observed for the electrode that had been coated with Ni for 20 s.
192 For increased sputter times, i.e. for the sample with t_s = 300 s, much higher roughness (~ 30 %)
193 and deformations (~ 160 %) were observed. Electrodes having t_{sp} = 60 s generally were very
194 similar to the behavior observed for bare TiO_2.
195

196 **Junction Energy Relations: AP-XPS**

197 TiO_2/(Ni) electrodes were examined by AP-XPS in a manner analogous to that described
198 previously [7], with Ni deposited for t_{sp} = 0 s, 20 s, 60 s, or 300 s, respectively. The binding energy,
199 E_B, of a core level can be calculated as $E_B = h\nu - E_{K,VAC} - \phi_{sample}$ where $E_{K,VAC}$ is the kinetic
200 energy of the photoelectron with respect to the vacuum energy level (E_{VAC}), ϕ_{sample} is the work
201 function of the sample, and $h\nu$ is the X-ray energy. E_B is measured relative to the Fermi energy,
202 E_F, of the analyzer (or of the sample, which are equal, because the two components are in
203 electrical contact). However ϕ_{sample} is unknown during the XPS measurements, and the kinetic
204 energy is referenced to the Fermi energy, E_F, if not otherwise noted, i.e. $E_K = E_{K,VAC} + \phi_{sample}$
205 (where ϕ_{sample} is the energetic difference between the E_{VAC} and the Fermi level of the sample).
206 This approach provides binding energies that are referenced to the analyzer. To provide a
207 description from an electrochemical perspective, we define E_B' as the core-level binding energy
208 referenced to the solution potential instead of referenced to E_F of the working electrode/analyzer.
209 Because the potentials are set at the working electrode with respect to the reference electrode, E_B'
210 can be defined by equation (1)

211 $$E_B' = E_B + qU_{eff} \quad (1)$$

212 where q is the absolute charge of an electron and U_{eff} tracks the difference in the electrochemical
213 potentials between the solution and the working electrode. U_{eff} is given by $U_{eff} = U - U_{fb}$ where U

214 is the applied potential and U_{fb} is the flat-band potential for the bare TiO_2 electrode (for details
215 see Ref. [7]). Hence the solution-corrected core-level binding energy, E_B', measures the binding
216 energy of a level relative to the solution potential. In this approach, the solution-corrected binding
217 energies E_B' of core levels of materials in solution, such as the O 1s level of solution (bulk) water,
218 should remain constant as the potential at the working electrode is varied (the effect of water in
219 the double layer is negligible at the ionic strengths used). Semiconductors that have "fixed" band
220 edges in a semiconductor/liquid junction should show no change in E_B' at the interface with a
221 change in U_{eff}, because in this picture, the band edges are fixed relative to the solution energetics.
222 However, for cases in which the band edges of the semiconductor shift, such as in the case of
223 accumulation or Fermi-level pinning due to defect states [7], the solution-corrected binding energy
224 would be expected to shift with respect to the solution potential. Thus when the binding energy is
225 referenced to the solution potential or to the potential of the reference electrode, the E_B' of the
226 water O 1s level and of the semiconductor/liquid junction semiconductor core levels would be
227 expected to be independent of the solution potential, and should exhibit a shift parameter
228 $\Delta' \equiv \partial E_B'/\partial U_{eff} = 0$ eV V^{-1}. However, for cases where the band edges shift with respect to the
229 solution, as may result from Fermi level pinning, a change in the solution-corrected binding
230 energies with solution potential is expected. This situation can be contrasted with the results
231 expected when the binding energies are determined with respect to the analyzer [7], because when
232 referencing binding energies to the analyzer (E_B), the water O 1s and pure (without metallization)
233 semiconductor/liquid junction semiconductor core levels are expected to show a shift
234 $\Delta \equiv \partial E_B/\partial U_{eff} = \Delta = -1$ eV V^{-1} with respect to the applied voltage [7].

235 Fig. 4 plots solution-corrected XPS spectra for the O 1s and Ti 2p core levels for a bare
236 TiO_2 electrode, in which the photoemission intensities are plotted against E_B', and Fig. 5 plots the
237 solution-corrected XPS spectra for the Ni 2p, O 1s and Ti 2p core levels of the TiO_2/Ni (20 s)

238 electrode vs E_B'. The bare TiO_2 XPS peaks showed less band-edge shifting whereas electrodes
239 with Ni showed a larger shift. Fig. 6a displays the full width at half maximum (FWHM) of the
240 liquid water O 1s core level, as well as of the TiO_2 O 1s peak, for the bare TiO_2 electrode. The
241 FWHM data are expected to reach a minimum at the flat-band potential [7]. Fig 6a shows that for
242 the bare TiO_2 electrode, the FWHM for the TiO_2 O 1s peak reaches a minimum at -0.9 V vs.
243 Ag/AgCl. Fig. 6b shows the solution-corrected core level shift for the Ti $2p_{3/2}$ core levels across a
244 range of potentials for the three different TiO_2/(Ni) electrodes. The slopes, Δ'_{Ti}, of the fitted lines
245 show that the solution-referenced binding energy E_B' of the Ti $2p_{3/2}$ core level shifted with a slope
246 of 1.0 ± 0.08 eV V^{-1} for TiO_2/Ni (20 s), 0.9 ± 0.10 eV V^{-1} for TiO_2/Ni (60 s), and
247 1.0 ± 0.07 eV V^{-1} for TiO_2/Ni (300 s). Fig. 6c shows that the relative peak shift, Δ'_{Ni}, of E_B' for
248 the Ni $2p_{3/2}$ core level for TiO_2/Ni (20 s) was 0.7 ± 0.07 eV V^{-1}; that for TiO_2/Ni (60 s) was
249 0.9 ± 0.08 eV V^{-1}; and the value for TiO_2/Ni (300 s) was 1.0 ± 0.08 eV V^{-1}. The errors associated
250 with these slopes result primarily from the resolution of, and uncertainty inherent to, the
251 measurement.

252 Fig. 7 displays XPS data showing the Ni $2p_{3/2}$ core level for samples prepared with
253 t_{sp} = 20 s, 60 s and 300 s. The electrode was maintained at a potential of -1.0 V vs. Ag/AgCl, and
254 the Ni(0), Ni(II), and Ni(III) peaks as well as the satellite peaks are labeled. A clear lack of a
255 metallic Ni phase was observed for the t_{sp} = 20 s sample at potentials positive of flat-band, and
256 only a very small amount of metallic Ni (6 %, Ni $2p_{3/2}$ peak area) was visible under reducing
257 conditions at U = -1.0 V vs. Ag/AgCl. In contrast, the t_{sp} = 60 s sample had a significant peak
258 area fraction (40%) of metallic Ni and the sample prepared using t_{sp} = 60 s showed a large
259 fraction (51 %) of metallic Ni. The Ni(III) content was 94 % for t_{sp} = 20 s, 47 % for t_{sp} = 60 s and
260 22 % for t_{sp} = 300 s, based on peak areas in the Ni $2p_{3/2}$ peak.

261

262 # Discussion

263 **Electrochemistry**

264 For lower Ni coverage, the electrode exhibited resistive behavior with very low currents
265 in both the KOH electrolyte and the $Fe(CN)_6^{3-/4-}$ redox solution (Fig. 2). However, currents
266 become substantial for the electrode that had t_{sp} =60 s (~ 2 nm) of Ni. The typical electrochemical
267 signatures of Ni oxidation and reduction as well as HER and OER were observed, with the
268 Ni(II)/(III) redox reaction showing irreversible behavior with a peak separation of 0.16 V.
269 Increasing t_{sp} to 300 s decreased this peak separation to 0.06 V, indicating that the conductivity of
270 the sample improved. Starting at the open-circuit potential and scanning toward more positive
271 potentials, the electrodes became covered with NiO, and then NiOOH, as evidenced by the
272 observation of a partial reduction of Ni(III) to Ni(II) (peak C, Fig. 2) in the cathodic branch of the
273 voltammetry. After several cycles in which the potential scan was stopped in the anodic waves,
274 the initially existing Ni metal had been partially oxidized. The corresponding current for Ni
275 oxidation was small because the successfully oxidized Ni overlayers inhibited further oxidation
276 of Ni metal. Prior XPS data on these 2 nm thick Ni films [7] support this conclusion by showing a
277 decrease in the Ni(0) signal with a concomitant increase in the Ni(II) signal. The increase in
278 sample conductivity for thicker Ni coverages is evident in Fig. 2b, where current densities
279 > 10 mA cm^{-2} are evident at +0.1 V vs. Ag/AgCl. Thus, the data show a distinct difference in the
280 sample conductivity depending on the amount of Ni deposited and on the anodization procedure
281 [12].

282

283 **AFM Microtopography**

284 Microtopography data indicated that for small t_{sp} values, the sample exhibited surface
285 roughness and a deformation of the bare TiO_2/solution interface. The dip in the deformation data

286 for the t_{sp} = 20 s sample suggests the presence of a different surface material than that observed
287 for either bare TiO_2 or for the thicker Ni-coated TiO_2 surfaces. This behavior is consistent with
288 expectations for a NiO_x/TiO_2 surface that does not contain underlying metallic Ni. The increasing
289 trend in deformation from t_{sp} = 20 s to t_{sp} = 300 s suggests that only after a 20 s deposition of Ni
290 did a substantial metallic phase exist at the TiO_2/NiO_x interface. This conclusion is also supported
291 by XPS data of the Ni 2p core level (Fig. 7).
292
293 **Energy relations by AP-XPS measurements**
294 The XPS technique integrates the signal over the spot examined in the experiment. Fig. 8
295 shows a schematic of the energy-band relations and the resulting description of the structures
296 considered herein. In the physical representation, the kinetic energies plus the work function, E_K,
297 of the photoelectrons are referred to the Fermi level E_F of the working electrode, which coincides
298 with that of the analyzer, to deduce E_B. In the electrochemical frame of reference, kinetic
299 energies are referred to the reference electrode potential to define E_B'. To be consistent, changes
300 in E_B' were measured with respect to the potential at which the flat-band condition was observed
301 for the bare TiO_2 electrode. This approach allows evaluation of the shift in the band edges with
302 respect to the solution potential as the applied potential is varied. If the shift in E_B' with potential
303 is greater than zero (see equation 1), band-edge movement occurs. Provided that the sampling
304 depth of the technique is smaller than the width of the space-charge region, the shift of E_B, Δ, and
305 of E_B', Δ', with potential should approximately be related by equation (2):
306 $$\Delta' = \Delta + 1 \text{ eV V}^{-1} \quad (2).$$
307 Hence, the semiconductor core levels in an ideal semiconductor/liquid junction will have
308 corrected peak shifts Δ', relative to the reference electrode, of $\Delta' = 0.0$ eV V^{-1}; the electrolyte will

309 also exhibit no shift; while the metal core levels in a pure metal/electrolyte junction will shift
310 with the full applied potential *relative to the reference electrode*, i.e. $\Delta' = 1.0$ eV V^{-1}.
311 Analysis of the electrochemical data alone does not directly allow assessment of whether
312 a rectifying or an ohmic contact was formed, because the high resistivity (t_{sp} = 20 s) could also be
313 observed for an isolated system that contains a buried Schottky barrier. The AP-XPS data,
314 however, enables this evaluation of the electrical properties of the materials in the device and at
315 the interfaces of interest.
316 As shown in Fig. 6b, the average solution-corrected binding energies of the Ti $2p_{3/2}$ core
317 level for the TiO_2/Ni (20 s) interface shifted by 1.0 eV V^{-1}; those for TiO_2/Ni (60 s) shifted by
318 0.9 eV V^{-1}; and those for TiO_2/Ni (300 s) shifted by 1.0 eV V^{-1}, all showing metal-like behavior.
319 For comparison, the band edges for bare TiO_2 were observed to shift only in the potential range
320 in which defect states occurred, and were otherwise stationary (at potentials more positive than
321 the conduction-band edge))[7], suggesting that the bare TiO_2 acts like a semiconductor outside of
322 the potential range where the defect states induce Fermi level pinning. Hence, the TiO_2/Ni (20 s),
323 TiO_2/Ni (60 s) and the TiO_2/Ni (300 s) electrodes all exhibited only small amounts of
324 rectification in the underlying TiO_2 layer. The improvements in observed conductivity (Fig. 2) of
325 the TiO_2/Ni electrodes in the order t_{sp} =0 s < 20 s < 60 s < 300 s therefore likely result from more
326 than simply the removal of rectification in the underlying TiO_2. Furthermore, as shown in Fig. 7,
327 the amount of interfacial metallic Ni increased significantly, with almost no Ni(0) present for t_{sp} =
328 20 s and half of the layer consisting of Ni(0) for t_{sp} = 300 s [24]. Hence, the data are consistent with
329 the presence of Ni, as opposed to NiO_x, at the TiO_2/Ni interface playing a dominant role in
330 determining the charge conduction through the device.
331 The importance of the Ni contact, as opposed to NiO_x, to the TiO_2, is evident based on the
332 combination of the electrochemistry (Fig. 2), the solution corrected Ti 2p and Ni 2p core level

333 shifts from AP-XPS data (Fig. 6), and the catalyst compositions (chemical states) from the
334 Ni $2p_{3/2}$ core level AP-XPS (Fig. 7). The bare TiO_2 sample is both nonconductive and observed to
335 be generally rectifying (Fig. 2 and 6), whereas the TiO_2 samples with substantial amounts of
336 metallic Ni ($t_{sp} \geq 60$ s) are ohmic at the semiconductor/liquid junction (i.e band-edge shifts of
337 $\Delta' \sim 1.0$ eV V^{-1}), and are electrically conductive, as evidenced by the *J-U* behavior. The sample
338 with the NiO_x layer ($t_{sp} = 20$ s) is, therefore, unique, in that it displays similar AP-XPS data in
339 that the band edges of the TiO_2 appear to be similarly disconnected from the solution, such that
340 they shift with respect to the solution potential, as is the case for the samples that have substantial
341 metallic Ni. However, the TiO_2 in the NiO_x-containing samples is nonconductive, as observed in
342 electrochemical analysis (Fig. 2). The junction between NiO_x and TiO_2 appears electronically
343 distinct from that between Ni and TiO_2 in that charge conduction is not present for the NiO_x/TiO_2
344 structure even though rectification at the TiO_2/liquid junction has largely been removed [24]. If a
345 purely conduction-band transport mechanism operates in the TiO_2, such that Ni metal is not
346 required to contact the TiO_2, the loss of rectification for the $t_{sp} = 20$ s sample should have allowed
347 for conduction to be observed for the device in contact with the $Fe(CN)_6^{3-/4-}$ redox solution.
348 Therefore, the lack of conduction in the samples for $t_{sp} = 20$ s is consistent with the presence of
349 NiO_x, as opposed to Ni, heavily influencing the electrical behavior of the TiO_2, leading to an
350 increase in resistivity and a consequent loss in film conductivity. The E_B for the Ti $2p_{3/2}$ core
351 level in the TiO_2/Ni samples with thick Ni was observed to be equal to that observed for the bare
352 TiO_2 films at a potential at the midpoint of the mid-gap states (459.0 eV to 459.1 eV), suggesting
353 an interplay between the mid-gap "defect" states and the Ni overlayer. These results are
354 summarized in Fig. 9 by the schematic energy diagrams of the solid/liquid interface. Fig. 9a-c
355 shows the situation for negative potentials *U* with respect to the flat-band condition, and Fig. 9d-f
356 depicts the situation for positive potentials *U* with respect to flat-band of the TiO_2/electrolyte

(Fig. 9a and 9d), TiO_2/NiO_x/electrolyte (Fig. 9b and 9e) and TiO_2/Ni/NiO_x/electrolyte (Fig. 9c and 9f) systems. In the presence of NiO_x and Ni, Fermi level pinning at the mid-gap states occurs. In the absence of Ni or NiO_x, TiO_2 develops a space-charge region with fixed band-edge positions outside of regions involving Fermi-level pinning or accumulation [7].

Conclusions

The results presented herein demonstrate that *operando* AP-XPS can be used to observe and quantify the degree to which catalysts influence the band energetics of underlying protection layers and the ECDL. In addition to providing information regarding the band energetics, layer composition and chemical state, AP-XPS also provides direct evidence regarding the nature of the rectification and contact at the interface. For various thicknesses of deposited Ni or NiO_x, the rectification in the underlying TiO_2 is mostly removed; however, the increase in conductivity for deposited Ni only occurs when the Ni phase contains a substantial amount of metallic Ni and not merely an oxide phase. As a result, the data indicate that the band lineups between the semiconductor and the metal or metal oxide overlayer, as well as electronic effects that result from this equilibration, are the crucial factors that induce conduction in the TiO_2 films under evaluation. Sufficiently dense metallization allows for stable conduction through such films.

Acknowledgments

This work was supported through the Office of Science of the U.S. Department of Energy (DOE) under award no. DE SC0004993 to the Joint Center for Artificial Photosynthesis, a DOE Energy Innovation Hub. The Advanced Light Source is supported by the Director, Office of Science, Office of Basic Energy Sciences, of the U.S. Department of Energy under Contract No. DE AC02

05CH11231. We thank Dr. Philip Ross for contributions to the conceptual development of the AP-XPS end station and experimental design.

382

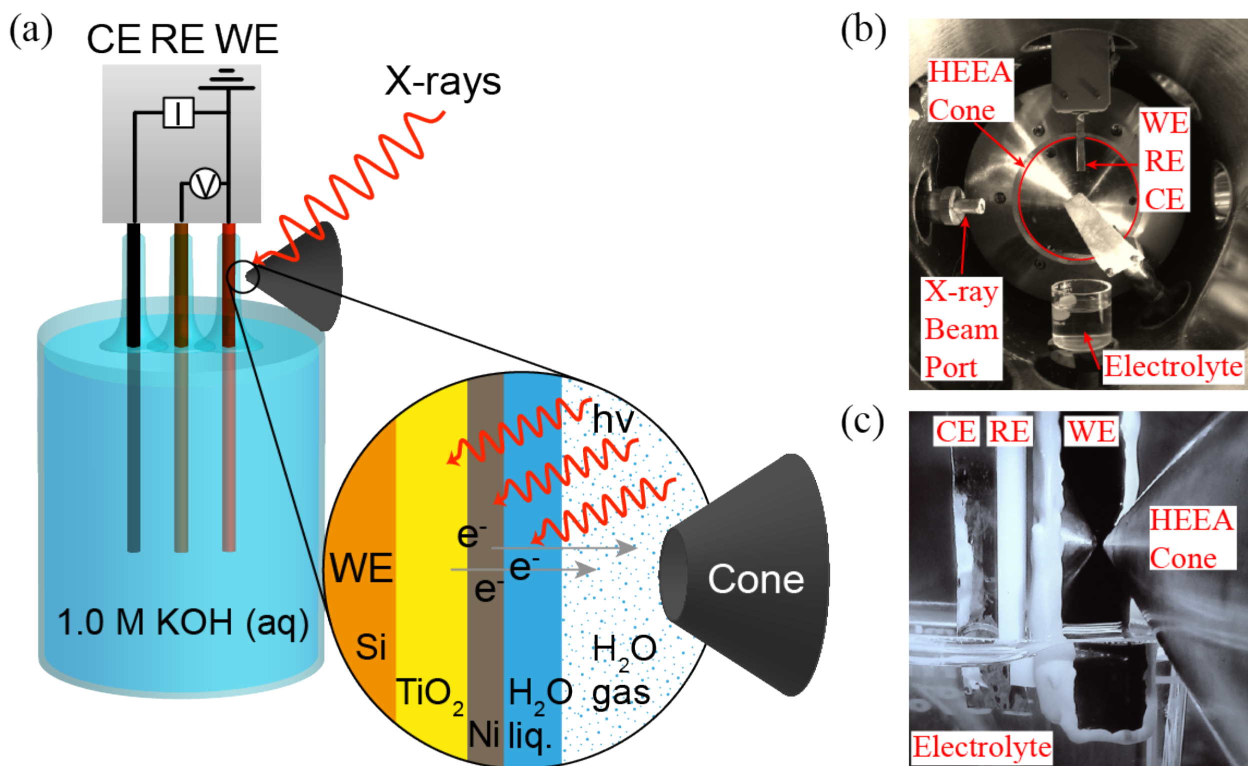

383 **Figure 1**: (a) Scheme of the *operando* XPS-PEC setup. The working electrode and the
384 hemispherical electron energy analyzer (HEEA) were grounded to each other. The potential of
385 the working electrode was changed with respect to the reference electrode. The PEC-beaker
386 containing the electrolyte could be moved in the z direction whereas the three-electrode mount
387 could be moved in the x-, y-, and z-directions. (b) View into the high-pressure analysis chamber.
388 The X-ray beam enters through the window on the left, the three-electrode setup is on the top, the
389 electrolyte beaker on the bottom, and the electron analyzer cone is in the center. (c) Three-
390 electrode setup pulled up and in measurement position (compare to (a)).

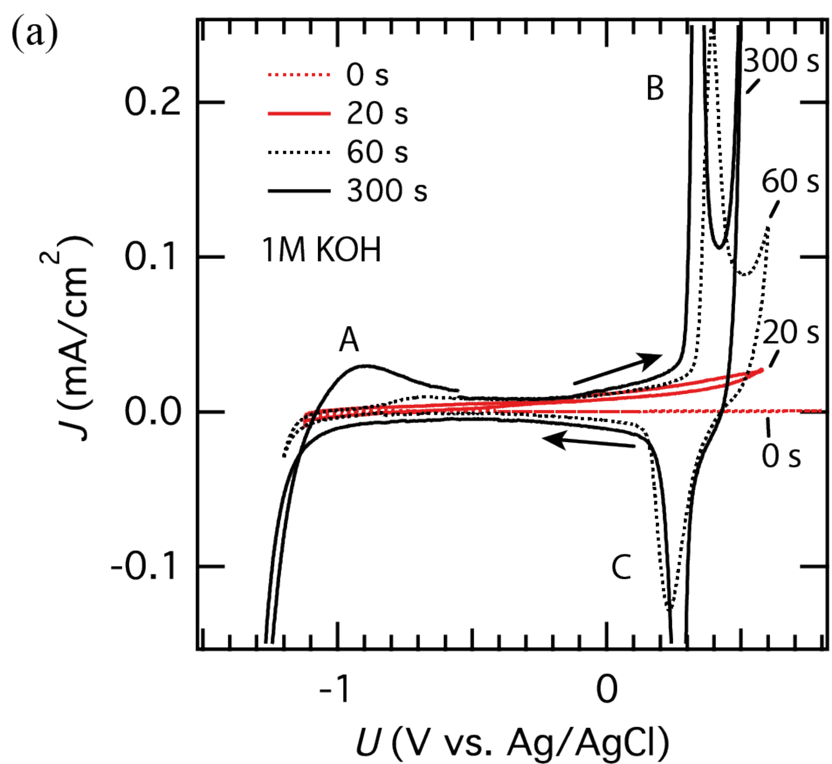

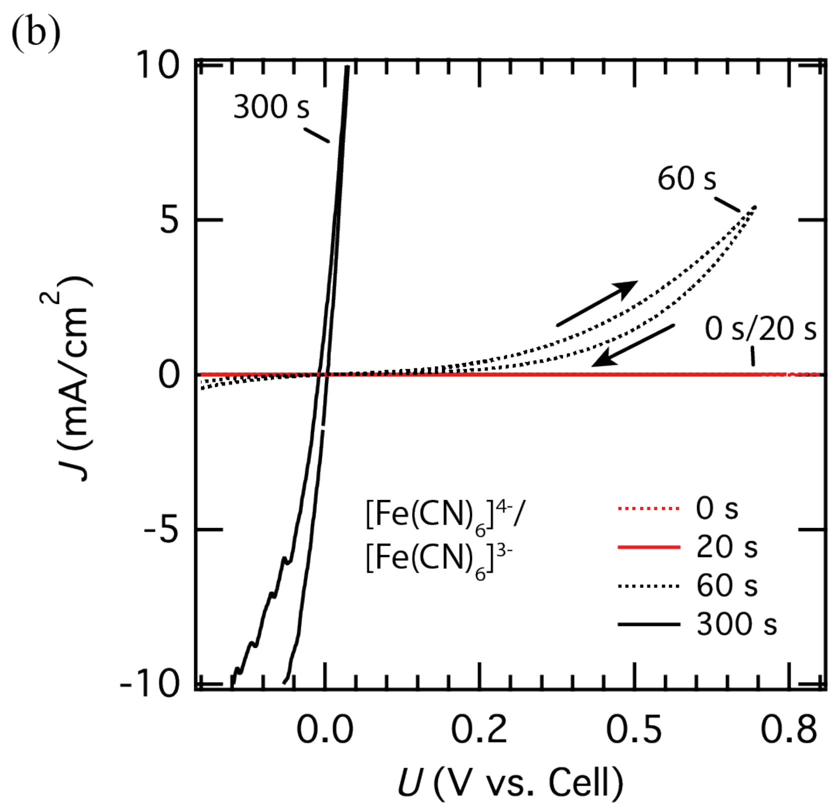

391

392 **Figure 2**: (a) *J-U* data collected for bare TiO_2, TiO_2/Ni (20 s), TiO_2/Ni (60 s), and

393 TiO_2/Ni (300 s) electrodes, respectively, in 1.0 M KOH(aq). Three peaks are observed: for

394 t_{sp} = 60 s, an anodic peak A at -0.7 V, an anodic peak B at +0.39 V, and a cathodic peak at

395 +0.23 V vs. Ag/AgCl. For t_{sp} = 300 s, these peaks shifted to -0.85 V, +0.34 V and +0.28 V vs.

396 Ag/AgCl. (b) *J-U* data measured in 50/350 mM $Fe(CN)_6^{3-/4-(}$aq) solution. Arrows show the scan

397 direction.

398

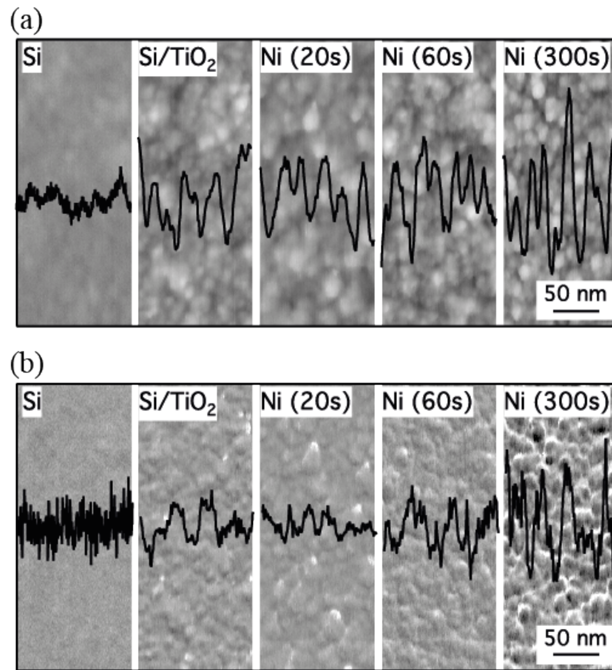

399 **Figure 3**: AFM microtopographs of bare silicon, ~ 70 nm thick TiO_2 on silicon, $Si/TiO_2/Ni$
400 (20 s), $Si/TiO_2/Ni$ (60 s), and $Si/TiO_2/Ni$ (300 s). (a) depicts the height information and (b) the
401 surface deformation by the AFM tip. The sub-micrographs in (a) and (b) have the same height
402 scaling. In each graph the insets show line scans from the middle of the microtopographs.

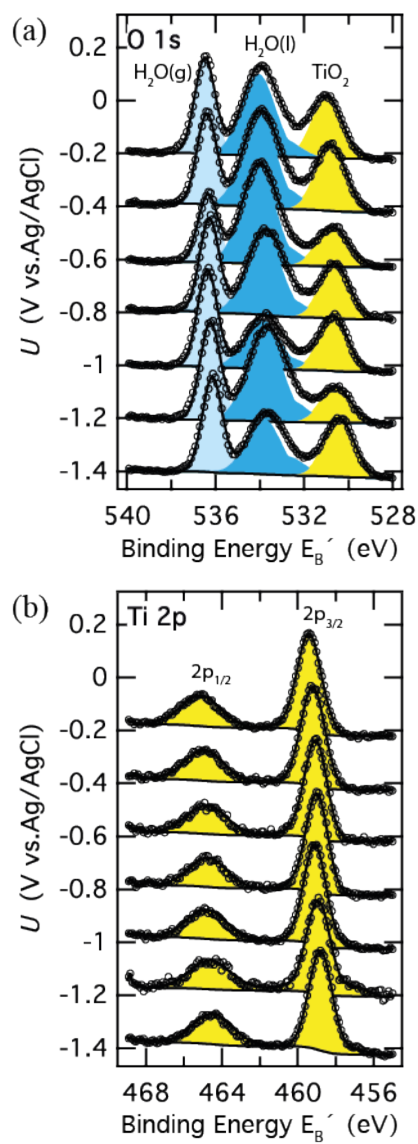

403

404 **Figure 4**: O 1s (a) and Ti 2p (b) X-ray photoemission spectra of the bare TiO_2 electrode in 1.0 M
405 KOH(aq) for U = -1.4 V to -0.2 V vs. Ag/AgCl. The binding energies are referenced to the
406 solution potential as explained in the text and corrected by the applied potential with respect to
407 flat-band conditions at U_{fb} = -0.9 V vs. Ag/AgCl [7].

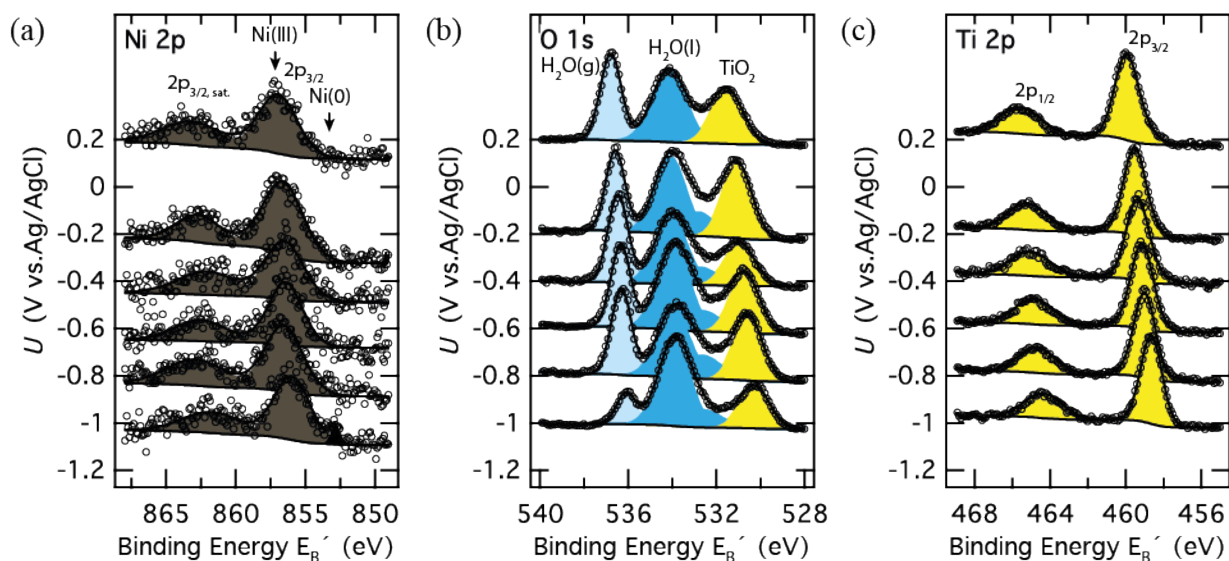

408

409 **Figure 5**: Ni 2p (a), O 1s (b), and Ti 2p (c) X-ray photoemission spectra of a TiO_2/Ni (20 s)
410 electrode in 1.0 M KOH(aq) for U = -1.0 V to +0.2 V vs. Ag/AgCl. The binding energies are
411 referenced to the solution potential as explained in the text and corrected by the applied potential
412 with respect to flat-band conditions at U_{fb} = -0.9 V vs. Ag/AgCl [7] (see Equation 1 and 2). The
413 positions of metallic (Ni(0)) and fully oxidized Ni (Ni(III)) are indicated in (a) by arrows.

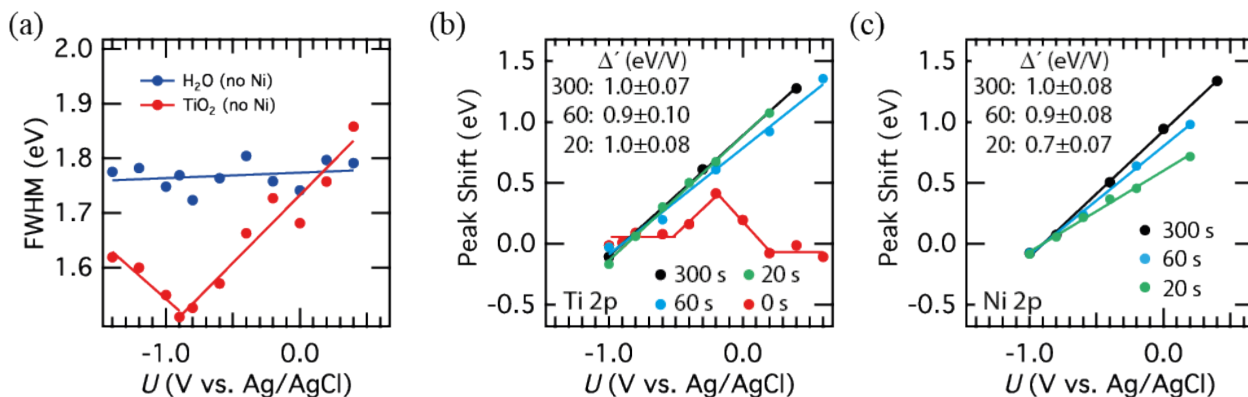

414

415 **Figure 6**: (a) Full width at half maximum (FWHM) peak data for the water O 1s and TiO_2 O 1s
416 core levels for a bare TiO_2 electrode. (b) The core level peak shifts with respect to the binding
417 energy at flat-band, which indicate the band-edge shift of the semiconductor with respect to the
418 electrolyte, of the Ti $2p_{3/2}$ core level for TiO_2/electrolyte, TiO_2/Ni (20 s)/electrolyte,
419 TiO_2/Ni (60 s)/electrolyte, and TiO_2/Ni (300 s)/electrolyte geometries. (c) Similar to (b) but
420 plotting only the Ni $2p_{3/2}$ core level peak shift for the t_{sp} = 20 s, 60 s, and 300 s electrodes. The
421 binding energies are referenced to the solution potential as explained in the text, and are corrected
422 by the applied potential with respect to flat-band conditions at U_{fb} = -0.9 V vs. Ag/AgCl [7] (see
423 Equation 1 and 2).

424

425

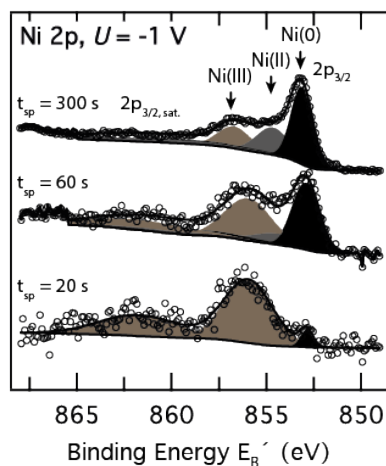

426 **Figure 7**: Ni $2p_{3/2}$ X-ray photoemission spectra for t_{sp} = 20 s, 60 s, and 300 s for U = -1 V vs.
427 Ag/AgCl. The binding energies are referenced to the solution potential as explained in the text
428 and corrected by the applied potential with respect to flat-band conditions at U_{fb} = -0.9 V vs.
429 Ag/AgCl [7] (see Equation 1 and 2). The positions of metallic (Ni(0)), Ni(II), and fully oxidized Ni
430 (Ni(III)) are indicated by arrows.

431

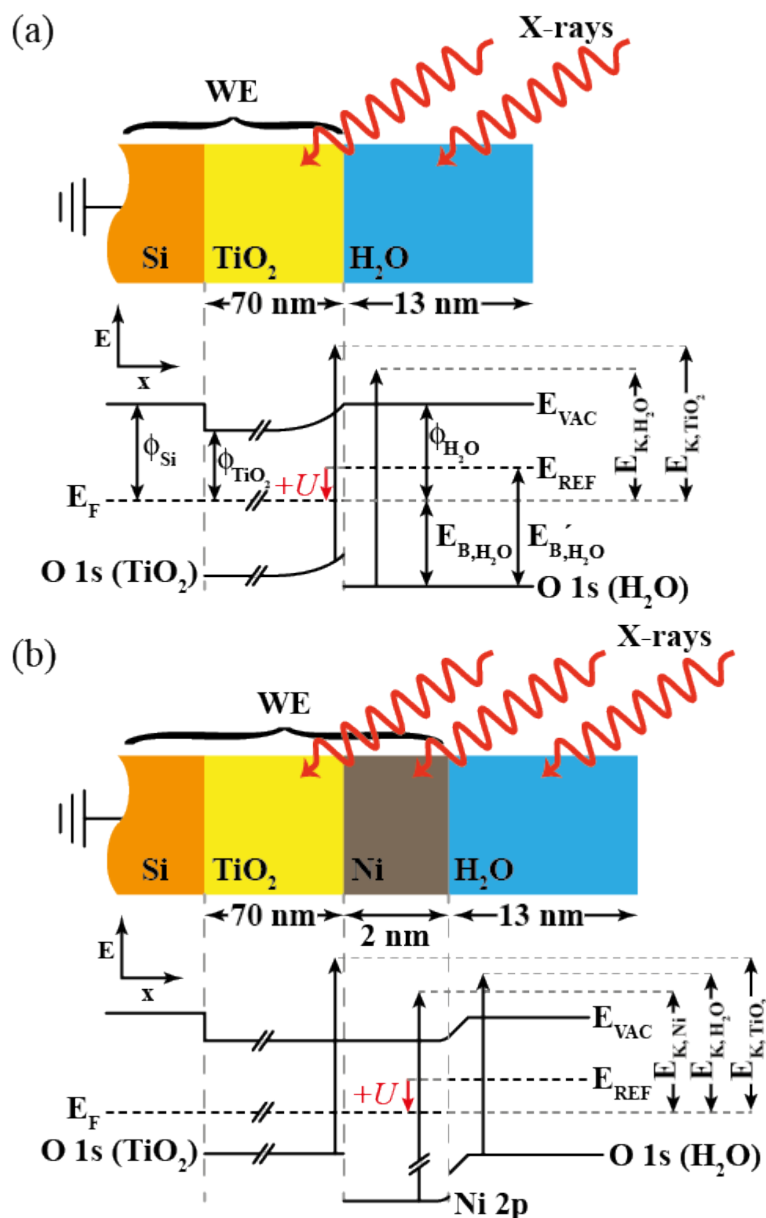

432

433 **Figure 8**: Scheme of the energy-band relations of *operando* photoelectron spectroscopy for (a)
434 the Si/TiO_2/electrolyte geometry and (b) the Si/TiO_2/Ni/electrolyte geometry. The working
435 electrode and analyzer are grounded. A potential is applied to the working electrode in the
436 electrolyte with respect to the reference electrode in a three-electrode configuration. The work
437 function of the material Φ is the difference between the Fermi energy, E_F, and the vacuum energy
438 E_{VAC}. The kinetic energies, $E_K = E_{K,VAC} + \Phi$, of the photoelectrons are measured with respect to
439 the Fermi energy of the analyzer. The binding energy, E_B, is calculated based the photon energy

440 with $E_B = h\nu - E_K = h\nu - E_{K,VAC} - \Phi$ whereas the binding energy with respect to the reference

441 electrode is $E_B' = E_B + qU_{eff}$ (Equation 1) as illustrated for the binding energy of the water O 1s

442 core level in (a).

443

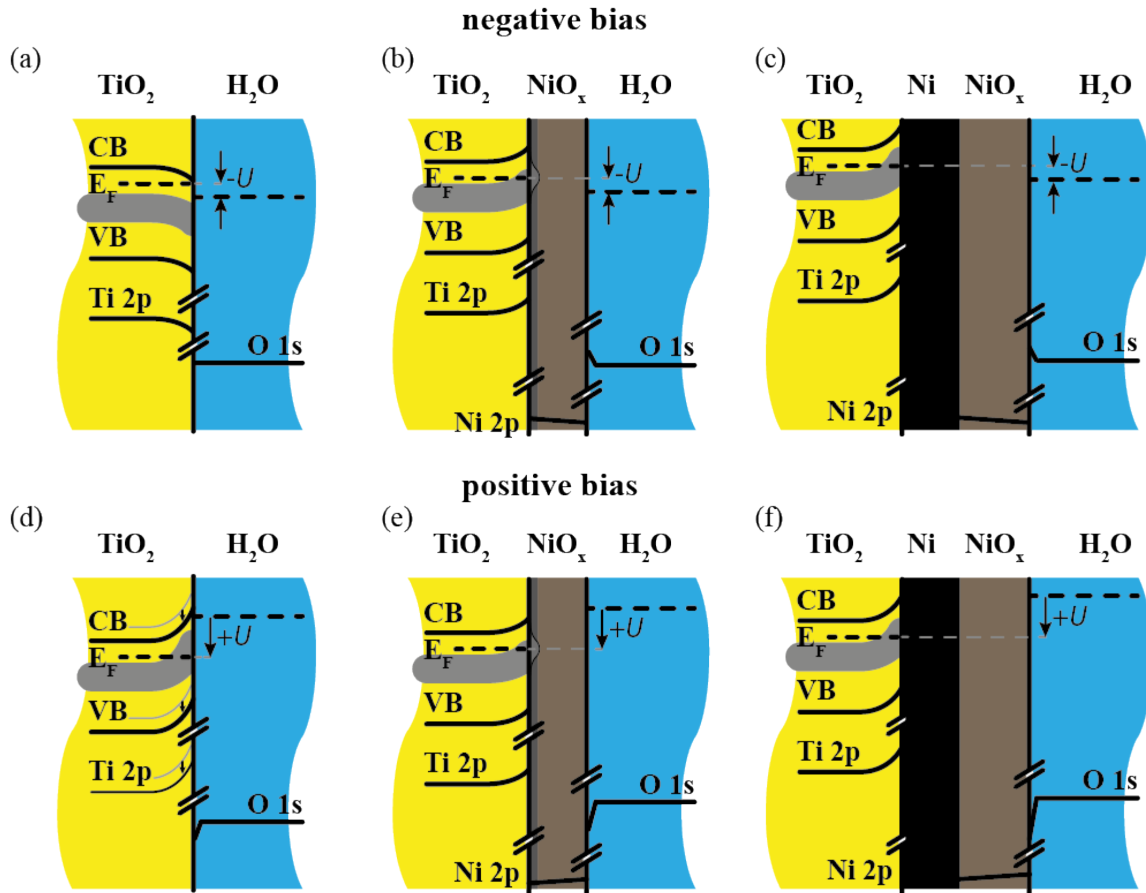

444 **Figure 9**: Band diagrams that summarize the experimental findings described herein. (a-c) for
445 negative potential *U* with respect to flat-band and (d-f) for negative potential *U* with respect to
446 flat-band. The thick grey line marks the position of the mid-gap state band in TiO_2. For (b, c and
447 e, f), Fermi level pinning at the mid-gap states occurs. (a, d) In the absence of Ni or NiO_x, TiO_2
448 develops a space-charge region with fixed band-edge positions outside of regions involving
449 Fermi-level pinning or accumulation [7]. For increasingly positive potentials, the Fermi level
450 crosses the mid-gap states and band edge shifting in TiO_2 is observed (indicated by the arrows).
451 The potential drop (the amount necessary to charge/discharge the surface states) occurs now in
452 the electrochemical double layer. (b, e) The Fermi energy at the TiO_2/NiO_x interface is pinned
453 near the mid-gap states due to NiO_x interface states [24]. With Fermi level pinning, the band edges
454 shift with the applied potential. (c, f) With a sufficiently dense and thick Ni film at the interface

455 to TiO_2, the TiO_2 band edges are effectively disconnected from the solution, and the presence of

456 metallic Ni allows for charge conduction.

457 **Table 1**: Surface roughness parameters obtained by AFM for the height distribution and the
458 surface deformation. While the surface roughness and deformation parameters stay nearly
459 constant up to 60 s (with a minimum for 20 s) the change (increase by up to 160 %) of the surface
460 properties is more drastic after Ni deposition with a 300 s sputter time.

Roughness / Ni	Height		Deformation	
	RMS (nm)	Ra (nm)	RMS (nm)	Ra (nm)
0 sec	0.71	0.55	0.17	0.12
20 sec	0.68	0.53	0.14	0.10
60 sec	0.69	0.55	0.17	0.13
300 sec	0.91	0.72	0.44	0.33

461

462 # References

463 1. H. Gerischer, *Journal of Electroanalytical Chemistry and Interfacial Electrochemistry*, **58**,
464 263–274 (1975).

465 2. Y. Ping, W. A. Goddard III, and G. A. Galli, *J. Am. Chem. Soc.*, **137**, 5264–5267 (2015).

466 3. H. J. Lewerenz, *J. Electrochem. Soc.*, **139**, L21–23 (1992).

467 4. H. J. Lewerenz, T. Bitzer, M. Gruyters, and K. Jacobi, *J. Electrochem. Soc.*, **140**, L44–L46
468 (1993).

469 5. K. Jacobi et al., *Phys. Rev. B*, **51**, 5437–5440 (1995).

470 6. S. Axnanda et al., *Sci. Rep.*, **5**, 9788–22 (2015).

471 7. M. F. Lichterman et al., *Energ. Environ. Sci.*, **8**, 2409–2416 (2015).

472 8. K. Sun et al., *Energy Environ. Sci.*, **5**, 7872–7877 (2012).

473 9. K. Sun et al., *P Natl Acad Sci Usa*, **112**, 3612–3617 (2015).

474 10. K. Sun et al., *Phys. Chem. Chem. Phys.*, **16**, 4612–4625 (2014).

475 11. Y. W. Chen et al., *Nat. Mater.*, **10**, 539–544 (2011).

476 12. S. Hu et al., *Science*, **344**, 1005–1009 (2014).

477 13. M. F. Lichterman et al., *Energy Environ. Sci.*, **7**, 3334–3337 (2014).

478 14. M. F. Lichterman et al., *Catal Today* (2015).

479 15. B. Mei et al., *J. Phys. Chem. C*, **119**, 15019–15027 (2015).

480 16. P. Reckers et al., *J. Phys. Chem. C*, **119**, 9890–9898 (2015).

481 17. M. T. McDowell et al., *ACS Appl. Mater. Interfaces*, **7**, 15189–15199 (2015).

482 18. B. Seger et al., *J. Mater. Chem. A*, **1**, 15089–15094 (2013).

483 19. Y. Lin et al., *J. Phys. Chem. C*, 150126152338001 (2015).

484 20. B. Seger et al., *Rsc Adv*, **3**, 25902–25907 (2013).

485 21. M. F. Lichterman et al., *ECS Transactions*, **66**, 97–103 (2015).

486 22. M. H. Richter et al., *ECS Transactions*, **66**, 105–113 (2015).

487 23. M. E. G. Lyons, R. L. Doyle, I. Godwin, M. O'Brien, and L. Russell, *J. Electrochem. Soc.*,
488 **159**, H932–H944 (2012).

489 24. M. H. Richter et al. (in preparation).

490